PCCP

DFT Investigation on the Adsorption of Munition Compounds on α-Fe_2O_3: Similarity and Differences with α-Al_2O_3

Journal:	*Physical Chemistry Chemical Physics*
Manuscript ID	CP-ART-04-2018-002590.R1
Article Type:	Paper
Date Submitted by the Author:	22-Jun-2018
Complete List of Authors:	Jenness, Glen ; U.S. Army Engineer Research and Development Center, Environmental Laboratory Seiter, Jennifer; U.S. Army Engineer Research and Development Center, Environmental Laboratory Shukla, Manoj; US Army Engineer Research and Development Center,

Journal Name

ARTICLE TYPE

Cite this: DOI: 10.1039/xxxxxxxxxx

DFT Investigation on the Adsorption of Munition Compounds on α-Fe_2O_3: Similarity and Differences with α-Al_2O_3†

Glen R. Jenness,* Jennifer Seiter, and Manoj K. Shukla*

Received Date
Accepted Date

DOI: 10.1039/xxxxxxxxxx

www.rsc.org/journalname

Arid environments have long been a testing and training ground for novel munitions. However, these activities leave behind unknown quantities of munition residues with unknown impact on local flora and fauna. In particular, arid soil contains Lewis acidic metal oxides which bind and catalyze the electron rich substituent groups commonly found in munition compounds, although the exact mechanisms are poorly understood. The current study remedies this lack of knowledge by utilizing density functional theory (DFT) to explore various orientations of four important munition compounds on the α-Fe_2O_3 (0001) and α-Al_2O_3 (0001) surfaces. Our findings reveal that while α-Fe_2O_3 binds the munition compounds more strongly than α-Al_2O_3, all four compounds experienced elongation of their nitro ($-NO_2$) groups, indicating their susceptibility towards degradation on these surfaces.

1 Introduction

Arid regions have long been used as a testing and training ground for novel munitions due to their remote nature. However, these activities can leave behind various quantities of munition compounds[1–4]. Arid regions contain a high concentration of oxide based minerals (*e.g.*, silicas, aluminas, ferric oxides etc.) which, under the right conditions, can act as a Lewis acid[5–9] and give rise to a situation under which the degradation of these compounds are catalyzed by the environment. The majority of the work on understanding the fate of munition compounds has focused either on the bulk compound in question[10] or in aqueous solution[11]. With the active development and potential testing of new munitions, it is critical that we understand how these compounds interact within the soil in order to determine their fate and transport.

Consequently, recent theoretical work has tried to answer the question of what transpires on the surface of common soil oxides. When adsorbed onto the α-SiO_2 (001) surface, it was found 5-amino-3-nitro-1H-1,2,4-triazole (ANTA) was more resistant to oxidation (as denoted by an increase in the oxidation potential) when compared to hydrated ANTA[12]. This is rather curious as SiO_2 is typically considered a "neutral" oxide[6]. Furthermore, it has been demonstrated experimentally that nitro ($-NO_2$) groups are readily transformed in the soil[13,14]. This trend of nitro group transformation has also been demonstrated for munitions such as TNT[15–17], RDX[17], DNAN[18], and dinitrophenol[19]. Thus whether or not the gain in stability in regards to oxidation for ANTA on the α-SiO_2 surface as shown by Sviatenko *et al.*[12] is transferable to the general case of ANTA in natural soil remains an open question.

Additionally, 5-nitro-2,4-dihydro-3H-1,2,4-triazol-3-one (NTO) is dissociatively adsorbed on the surface of α-Al_2O_3 (0001), with a proton being transfered to a surface oxygen and the preferred binding orientation is a vertical binding mode through the electron rich carbonyl and nitro groups. An accumulation of charge density at the center of bond between the Al^{+3} metal site and the adsorbate was also observed[20]. However, 2,4,6-trinitrotoluene (TNT) prefers to bind to the surface in a parallel orientation with no dissociation of the molecular bonds[21]. Furthermore, nitroguanidine (NQ) and 1,1-diamino-2,2-dinitroethylene (FOX7) prefers the parallel binding orientation on the α-Al_2O_3 (0001) surface[22]. Based on charge density differences, complexes of TNT, NQ, and FOX7 with α-Al_2O_3 all experienced a depletion of charge at the binding centers and accumulation of charge at the center of the adsorbate-surface bond[20–22].

The current study seeks to increase our knowledge regarding the fate of munition compounds in soil by studying the nature of the adsorption of four munition compounds, *i.e.*, TNT, 2,4-dinitroanisole (DNAN), NTO, and NQ (with the last three being insensitive munition compounds) on the α-Al_2O_3 (0001) and α-Fe_2O_3 (0001) oxide surfaces through the application of den-

Environmental Laboratory, US Army Engineer Research and Development Center, 3909 Halls Ferry Road, Vicksburg, Mississippi 39180, United States. E-mail: Glen.R.Jenness@usace.army.mil; Manoj.K.Shukla@usace.army.mil

† Electronic Supplementary Information (ESI) available: Tables and figures containing the numerical values of the energetics plotted in the current study are provided. See DOI: 10.1039/b000000x/

sity functional theory (DFT). Several Lewis acid properties were calculated utilizing DFT, and our results show that α-Fe_2O_3 is a stronger Lewis acid than α-Al_2O_3, and as a consequence should experience stronger interactions with the munition compounds. Utilization of the minima hopping algorithm[23,24] revealed the presence of 509 distinct binding orientations. Calculation of the binding energies for each orientation confirms the munition compounds interact more strongly on the α-Fe_2O_3 (0001) surface than the α-Al_2O_3 (0001) surface. However, adsorption on both surfaces results in an elongation of the N–O bonds in the nitro (–NO_2) group(s). Analysis of the density of states for these compounds shows the –NO_2 groups are comprised largely of bonding interactions near the highest occupied molecular orbital; consequently depletion of charge from this region is responsible for the observed elongation. In line with previous experimental observations[13–19], our results indicate that the –NO_2 group(s) are susceptible to being transformed into amine (–NH_2), nitroso (–NO), or –NOOH groups and provides a rationale for this trend utilizing the Lewis acid properties of the surface.

2 Methods

2.1 Computational Methods

All density functional theory calculations were performed with the GPAW[25] *ab initio* program within the Atomic Simulation Environment (ASE)[26]. Valence electrons were represented with a real-space grid basis set[27] (with a spacing of 0.2 Å) with the electron exchange and correlation being approximated with the the Perdew-Burke-Ernzerhof (PBE) exchange-correlation functional[28]; the core electrons were represented via the real-space implementation of the projected augment wavefunction (PAW) method[27,29,30]. Total energies were minimized self consistently using the RMM-DIIS method[31,32] to a convergence threshold of 10^{-6} eV. To prevent discontinuities at the Fermi level, the Fermi-Dirac smearing method was employed with a smearing parameter of 0.1 eV. Calculations involving the α-Fe_2O_3 (0001) surface were spin-polarized, with a Hubbard-*U* parameter of 3.8 eV applied to the *d*-orbitals of the Fe atoms[33]. As spin does not affect the energetics of the α-Al_2O_3 (0001) surface, spin was ignored for this surface.

Initial binding orientations were generated using the minima hopping algorithm of Goedecker[23] as implemented in ASE[24]. Briefly, minima hopping starts a molecular dynamics run in the NVE (microcanonical) ensemble; following a short run (typically 20-25 fs), the geometry is then minimized and compared to previously found geometries. If the new geometry is sufficiently different, it is then stored in a list of accepted minima; otherwise it is discarded. This procedure is then repeated until a certain number of minima have been explored (here, all minima hopping runs are terminated until a total of 40 minima have been found). In order to preserve the molecular identity of each adsorbate, the chemical bonds were represented via a Hookean constraint[24], with critical distance and spring constants being chosen to prohibit extraneous motion whilst still allowing for the bonds to change length. During the minima hopping procedure, the geometries were optimized with the limited memory Broyden-Fletcher-Goldfarb-Shanno (LBFGS) method[34] to a force convergence of 0.15 eV $Å^{-1}$, with the MD and optimization steps utilizing a double-ζ plus polarization LCAO basis set[35] with the reciprocal space sampled at the Γ-point. Additionally, the surface atoms were held fixed in order to prevent the movement of surface atoms dominating the potential energy surface. While efficient, this procedure still incurs a significant computational cost; thus, the minima hopping was done with a smaller $p(2\times2)$ surface. Once the unique structures were found, the adsorbate was transferred to a $p(4\times4)$ surface and fully optimized by removing the Hookean constraints, and unfreezing the top stoichiometric layer of the surface (where a stoichiometric layer is defined as a layer of either Fe or Al, and two layers of oxygen). Geometries were optimized to a force convergence of 0.05 eV $Å^{-1}$ using the LBFGS optimizer and a DZP basis set. A subsequent optimization using a finite-difference basis set with a grid spacing of 0.20 was then performed. This procedure generated a total of 509 unique binding orientations.

Once the structures are fully optimized with the above methodology, the binding energies were calculated in the standard fashion, *i.e.*,

$$E_{\mathrm{BE}} = E_{\mathrm{ads+surface}} - E_{\mathrm{ads}} - E_{\mathrm{surface}}, \tag{1}$$

where $E_{\mathrm{ads+surface}}$ is the total energy of the adsorbate and oxide surface, E_{ads} is the gas-phase adsorbate energy, and E_{surface} is the energy of the bare oxide surface. Thus, from Equation 1, a more negative binding energy corresponds to a stronger interaction between the surface and the adsorbate. For structures where the adsorbate is deprotonated, the binding energy was still computed using Equation 1 where the neutral form of the adsorbate was used. It should be noted that this is a common practice in the calculation of the binding energy on oxide surfaces[36]. Given this definition of the binding energy, we calculated the mean binding energy as

$$\overline{E}_{\mathrm{BE}} = \frac{1}{N}\sum_{i=0}^{N} E^{i}_{\mathrm{BE}}, \tag{2}$$

where *i* denotes an orientation generated from the minima hopping and *N* is the total number of orientations for that binding geometry. Following calculation of the mean, the standard deviation (σ) can also be calculated,

$$\sigma = \sqrt{\frac{1}{N}\sum_{i=0}^{N}\left(E^{i}_{\mathrm{BE}} - \overline{E}_{\mathrm{BE}}\right)^2}. \tag{3}$$

A Bader charge analysis[37] as implemented by Henkelman and co-workers[38–40] was carried out for the lowest energy structures. Finally, the electronic structure of each adsorbate at their respective minimum was analyzed via the crystal orbital overlap population (COOP)[41] analysis, which weighs the density of states (DOS) with a Mulliken factor,

$$\mathrm{COOP}(\varepsilon) = 2\sum_{n}\sum_{k} c_i^* c_j S_{ij}\,\delta(\varepsilon - \varepsilon_n(\mathbf{k})), \tag{4}$$

where $c_{i/j}$ are the coefficients of atom i/j, S_{ij} is the overlap matrix between atoms *i* and *j*, *n* denotes the band, *k* denotes the relevant *k*-point, and $\delta(\varepsilon - \varepsilon_n(\mathbf{k}))$ is the delta function responsible

for the DOS. Peaks where COOP are negative denote anti-bonding orbitals, whilst positive peaks represent bonding orbitals; regions where the peak is zero (compared to the standard DOS) denote orbitals that are non-bonding[41].

2.2 Surfaces

Table 1 Lattice parameters for bulk $p(\mathbf{1}\times\mathbf{1}\times\mathbf{1})$ α-Al_2O_3 and α-Fe_2O_3 (units in Å).

Oxide	Method	a	c	Reference
	PAW, PBE	4.7844	13.0286	Current Study
α-Al_2O_3	Ultrasofts, PBE	4.7674	13.0128	Skukla and co-workers[20,21]
	Experiment	4.7602	12.9933	Lewis *et al.*[42]
	PAW, PBE+U	5.1436	13.7305	Current Study
α-Fe_2O_3	PAW, PW91+U	5.1230	13.8920	Rivera *et al.*[33]
	Experiment	5.0355	13.7471	Maslen *et al.*[43]

Bulk α-Fe_2O_3 and α-Al_2O_3 have a hexagonal lattice, belonging to spacegroup $R\bar{3}c$ (#161). For α-Fe_2O_3, we assumed a ferromagnetic spin state. Lattice constants were optimized utilizing the `GPAW` code; however, as analytical stresses are not available with either the LCAO or finite difference basis sets, the requisite stresses were calculated using a planewave basis set with a energy cutoff of 600 eV, and the reciprocal space being sampled with a $(3\times3\times3)$ Monkhorst-Pack grid[44]. A similar setup has previously been used, and it has been sufficient for generating lattice parameters[36,45,46]. A comparison of lattice parameters generated in the current study to prior work is shown in Table 1. We find good agreement with experiment for α-Al_2O_3. However, our setup resulted in an extended a parameter for α-Fe_2O_3. As our parameters are similar to prior computational results utilizing a PAW pseudopotential[33], we deem the a parameter to be sufficient for the current study.

Following the optimization of the unit cell parameters, the (0001) surface of each oxide was considered. Each of the surfaces generated are composed of three stoichiometric layers (with each stoichiometric layer containing a layer of either Al or Fe, and two layers of oxygen) and are shown in Figure 1. As prior work from our group utilized a surface model with six stoichiometric layers[20–22], we compared the binding energy of the first five flat orientation of TNT on the α-Fe_2O_3 (0001) surface from the three layer model to the six layer model with the results shown in Table S1, ESI†. From here, we can see that increasing the surface thickness has a mild impact on the binding energy ($\Delta E_{BE} < 0.1$ eV) with the exception of the flat 2 orientation. These results are in line with prior work on the α-Al_2O_3 surface by one of the current authors[45]. Thus, we view the thinner surface used in the current study as a good trade off between accuracy and computational efficiency.

3 Results

3.1 Characterization of Lewis acidity

It is well known that metal sites in metal oxides act as Lewis acids[6,47]; thus, it is instructive to consider the Lewis acid properties of the α-Al_2O_3 and α-Fe_2O_3 surfaces before discussing their interaction with various munition compounds. Here, we will be examining the core functionality of a Lewis acid, *i.e.* its ability to accept charge from a Lewis base (*i.e.*, the munition compounds in Figure 3). It has been shown a useful measure of the Lewis acidity is the mean of the *s*-conduction band,

$$E_s^* = \frac{\int_{\varepsilon_F}^{\infty}\rho_s(\varepsilon)\varepsilon d\varepsilon}{\int_{\varepsilon_F}^{\infty}\rho_s(\varepsilon)d\varepsilon}, \quad (5)$$

where ε_F is the Fermi level (taken to be the energy of the highest occupied band), $\rho_s(\varepsilon)$ is the energy-dependent *s*-orbital contribution from the projected density of states (PDOS), and ε is the energy[45]. The projected density of states with the E_s^* marked is shown in Figure 2. In addition to the electronic factor presented in Equation 5, we also consider the binding of a probe molecule to the α-Al_2O_3 and α-Fe_2O_3 surfaces; here, we chose carbon monoxide (CO) as it is a common experimental probe of Lewis acidity[6,48]. The results of these calculations are presented in Table 2.

Table 2 Lewis acid properties of the α-Fe_2O_3 (0001) and α-Al_2O_3 (0001) surfaces.

Oxide	E_s^* (eV)	E_{BE}^{CO} (eV)	ΔQ_{CO} (me^-)
α-Al_2O_3 (0001)	5.60	−0.74	36.68
α-Fe_2O_3 (0001)	3.88	−1.45	85.38

Comparison of the E_s^* values reveals that the mean of the *s*-conduction band for α-Al_2O_3 is $\sim 1.5\times$ greater than for α-Fe_2O_3. As Equation 5 represents the solid Lewis acid equivalent of the well known highest occupied molecular orbital (HOMO)–lowest unoccupied molecular orbital (LUMO) gap used to characterize non-solid Lewis acids, we can apply the following physical description to this result: a lower E_s^* indicates the conduction band is closer to the Fermi level, which facilitates the transfer of electrons from the HOMO of the adsorbate (by definition located near the Fermi level of the adsorbate-surface system) into the conduction band[45]. In other words, a strong Lewis acid would have a smaller E_s^* when compared to a weaker Lewis acid. Thus, examination of the E_s^* values in Table 2 indicates α-Fe_2O_3 would act as a stronger Lewis acid than α-Al_2O_3.

Moreover, it is well known that the stronger an adsorbate binds to the surface, a greater degree of overlap between the bands of the surface and the molecular orbitals of the adsorbate exist[49]. As charge-transfer interactions (*e.g.*, Lewis acid-base interactions) are proportional to the orbital overlap[50], we can state that Lewis acids that bind a probe molecule more strongly would have a greater amount of acidity compared to those that bind it more weakly[48]. Thus, consideration of the CO binding energy $\left(E_{BE}^{CO}\right)$ in Table 2 will provide further insight into the relative Lewis acidities of the two oxides; here, the E_{BE}^{CO} of α-Fe_2O_3 is $\sim 2\times$ that of α-Al_2O_3 in magnitude, which substantiates the E_s^* results discussed above. Further substantiation is provided via the change in the Bader charge of CO (ΔQ_{CO}); from Table 2, it is readily apparent that while both surfaces gained charge density (denoted via the positive ΔQ_{CO}), α-Fe_2O_3 (0001) gained $\sim 2.3\times$ more charge density than the α-Al_2O_3 (0001) surface.

Based on the above analysis of the Lewis acidity, it is expected

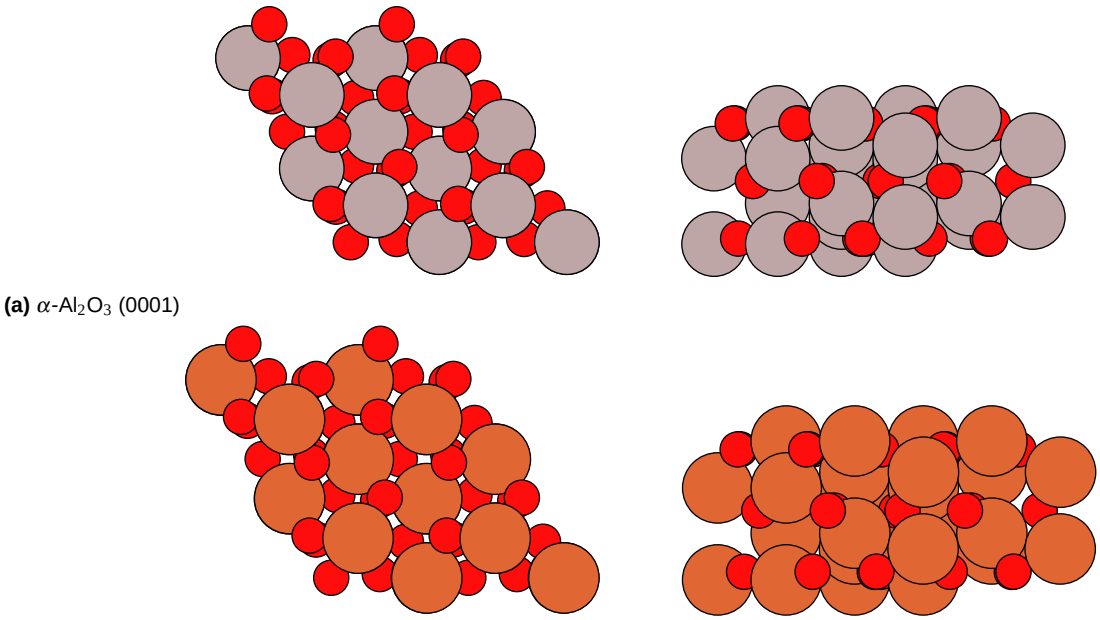

(a) α-Al_2O_3 (0001)

(b) α-Fe_2O_3 (0001)

Fig. 1 Top and side views of the (a) α-Al_2O_3 (0001) and (b) α-Fe_2O_3 (0001) surfaces. Oxygens are denoted as red circles, aluminum as gray, and iron as orange.

that the α-Fe_2O_3 (0001) surface would bind the munition compounds shown in Figure 3 more strongly than that of the α-Al_2O_3 (0001) surface. We anticipate an elongation of the chemical bonds in the electron rich substituent groups to occur more strongly upon adsorption to the α-Fe_2O_3 surface, and as a consequence their transformation should occur more readily on α-Fe_2O_3 than α-Al_2O_3.

3.2 Binding of munition compounds to soil oxides

3.2.1 2,4,6-Trinitrotoluene (TNT) and 2,4-Dinitroanisole (DNAN)

Table 3 Charge transferred from the munition compounds 2,4,6-trinitrotoluene (TNT), 2,4-dinitroanisole (DNAN), 5-nitro-2,4-dihydro-3H-1,2,4-triazol-3-one (NTO), and nitroguanidine (NQ) to the oxide surfaces (units in millielectrons, me^-); most stable configuration for each mode was used.

Molecule	Binding orientation	Charge transferred	
		α-Al_2O_3	α-Fe_2O_3
TNT	Mode 1	102	148
	Mode 2	97	137
	Flat	138	300
DNAN	Mode 1	89	93
	Mode 2	88	111
	Flat	157	233
NTO	Mode 1	63	167
	Mode 2	104	128
	Flat[a]	269	299
NQ	Mode 1	34	70
	Mode 2	40	283
	Flat[a]	27	114

[a] Here, flat refers to the initial configuration.

We begin our discussion by considering the effect of α-Fe_2O_3 and α-Al_2O_3 on 2,4,6-trinitrotoluene (TNT). As TNT is a cyclic aromatic, it can bind to the surface in a "flat" configuration, *i.e.* the plane of the aromatic ring is parallel to the surface. Additionally, TNT has two unique nitro (–NO_2) groups that are available for binding to a Lewis acid M^{+3} site; these groups are labeled as mode 1 and mode 2 (with mode 2 have an equivalent symmetric site) in Figure 3a. Given the structural similarities it would be interesting to compare TNT with the insensitive muntion 2,4-dinitroanisole (DNAN). Similar to TNT, DNAN has a cyclic aromatic ring that is available for binding in a flat configuration along with additional modes involving the two nitro groups. DNAN features a methoxy group which does carry lone electron pairs that are (in principle) available for binding. However a binding mode through this atom was not found due to the steric hindrances imposed by the methyl and benzyl moieties.

Comparison of the mean binding energies shown in Figures 4b and 5b reveals that the α-Fe_2O_3 (0001) surface binds both molecules more strongly than α-Al_2O_3, (0001) surface and the results are in line with the predicted Lewis acid strengths we discussed in Section 3.1. Furthermore we note that for both surfaces the flat mode of DNAN shows a larger standard deviation in the mean binding energies than what is observed for TNT. From Figures S14b and S26b of the ESI† it is evident that the methoxy group results in a slightly tilted configuration that is not seen for TNT (Figures S11b and S23b). Examination of the geometries generated *via* the minima hopping algorithm reveals that this slight elevation allows for the methoxy group to rotate about the C–O bond. When the methoxy is oriented towards the *ortho* –NO_2 (C_4–C_5) group, the binding energy is ∼0.8 eV weaker compared to the configurations where the methoxy group is oriented away from the *ortho* –NO_2 group. Thus, we attribute the larger

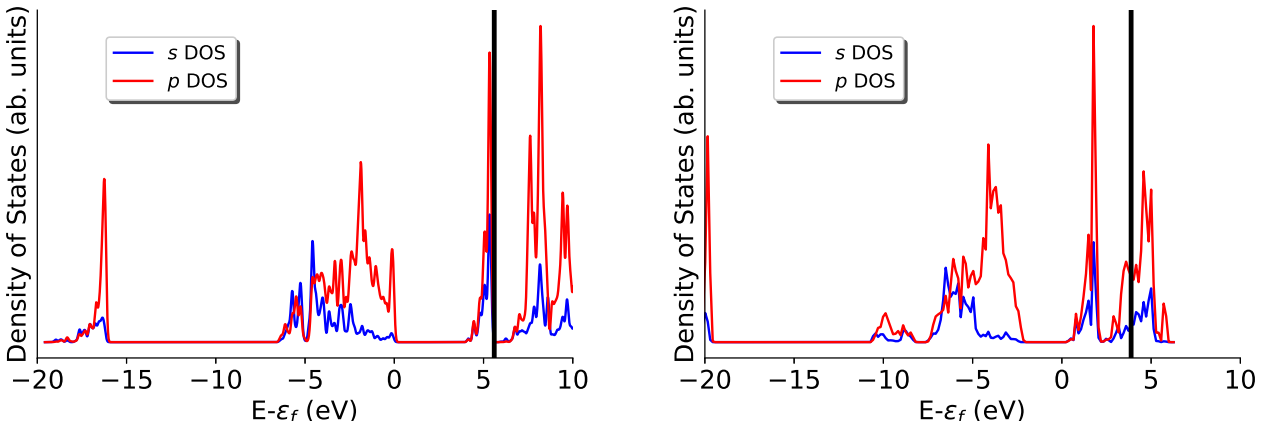

(a) α-Al_2O_3 (0001) **(b)** α-Fe_2O_3 (0001)

Fig. 2 Projected density of states for M^{+3} binding site on the (a) α-Al_2O_3 (0001) and (b) α-Fe_2O_3 (0001) surfaces. Energy is zeroed to the Fermi level (taken to be the energy of the highest occupied band), with the vertical black lines denoting the position of the E_s^* energy.

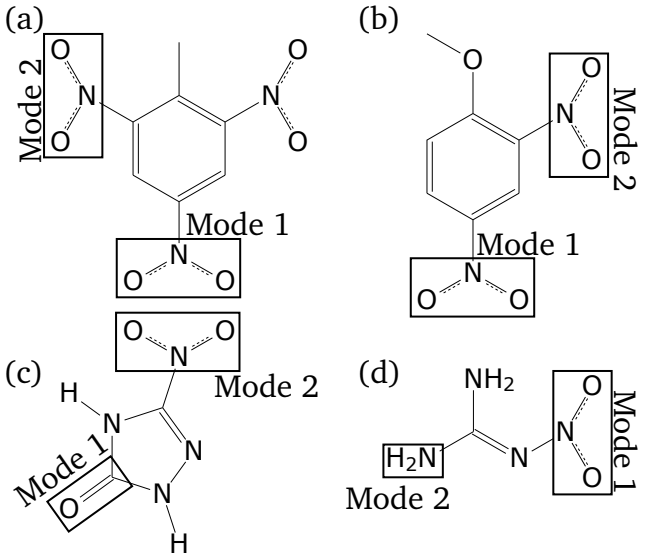

Fig. 3 Munition compounds with the binding modes labeled: (a) 2,4,6-trinitrotoluene (TNT), (b) 2,4-dinitroanisole (DNAN), (c) 5-nitro-2,4-dihydro-3H-1,2,4-triazol-3-one (NTO), and (d) nitroguanidine (NQ). A third binding mode for each compound is also considered; denoted in the current study as "flat", this mode places the plane of the compound parallel to the (0001) plane of each oxide surface.

standard deviation for DNAN to the rotational flexibility of the methoxy group.

Comparison of our binding energies for TNT on α-Al_2O_3 with those from Shukla and Hill reveal that our binding energies are ~0.3 eV lower in magnitude[21]. This difference can be attributed to the use of different pseudopotentials in the current study (PAW's in the current study vs. ultrasofts in the prior). Moreover, the current study focuses on the mean binding energy for a variety of configurations while earlier investigations only considered the binding energy from a single configuration. However, it should be noted that similar to Shukla and Hill, we find that the Lewis acid M^{+3} site is displaced upwards from the surface in the presence of both TNT and DNAN when compared to that of the clean surface[21]. This is easily rationalized in terms of the coordination of the M^{+3} site; as surface atoms are typically electron deficient due to the decrease in coordination, these atoms are pulled closer to the more bulk-like atoms. Upon adsorption, electrons are donated to the surface atoms which allow for a partial compensation in the coordination number[51]. As a consequence, the M^{+3} sites that are coordinated to a munition compound will be displaced out of the plane of the surface.

Table 3 reports the amount of charge density that is transferred from TNT and DNAN to the oxide surface for the lowest energy structures. From this table, it is readily apparent that the munition compounds when adsorbed on the oxide surface loses charge density to the Lewis acid M^{+3} site. Furthermore, TNT donates more charge density than DNAN, which is attributed to the presence of the extra $-NO_2$ group on TNT, which results in the formation of another coordination with the surface metal atoms than what is seen for DNAN. As can be seen from the bond length changes in Figure 6 and Tables S3–S8 of the ESI†, an elongation of the N–O bond occurs for the $-NO_2$ groups near the M^{+3} Lewis acid site. Curiously, modes 1 and 2 show the C–N bond contracting, with TNT showing the greater degree of contraction compared to DNAN, as shown in Figure 6. The trends in bond changes are readily apparent from an analysis of the COOP curves in Figures 4c and 5c; here we see the HOMO level for the N–O bonds is largely bonding in nature. Thus, as charge density from this orbital is depleted, the bond order would decrease, and as a result elongation of the bond occurs.

Comparison of Figures 4c and 5c reveals that near the HOMO level, the C–N bonds have more of a bonding character. Moreover, a direct comparison between the COOP for TNT and DNAN shows TNT having the greater anti-bonding character near the HOMO, and therefore we expect the C–N bonds in this molecule to contract more, which is observed by comparison of Tables S3, S4, S6, and S7 of the ESI†. These changes are readily visualized *via* a charge density difference, as shown in Figures S1 and S5 of the ESI† for TNT, and Figures S2 and S6 of the ESI† for DNAN. Here, we can readily see that the N–O bonds have a depletion of charge (denoted by the blue regions), while the C–N bonds accumulate charge (denoted by the yellow regions).

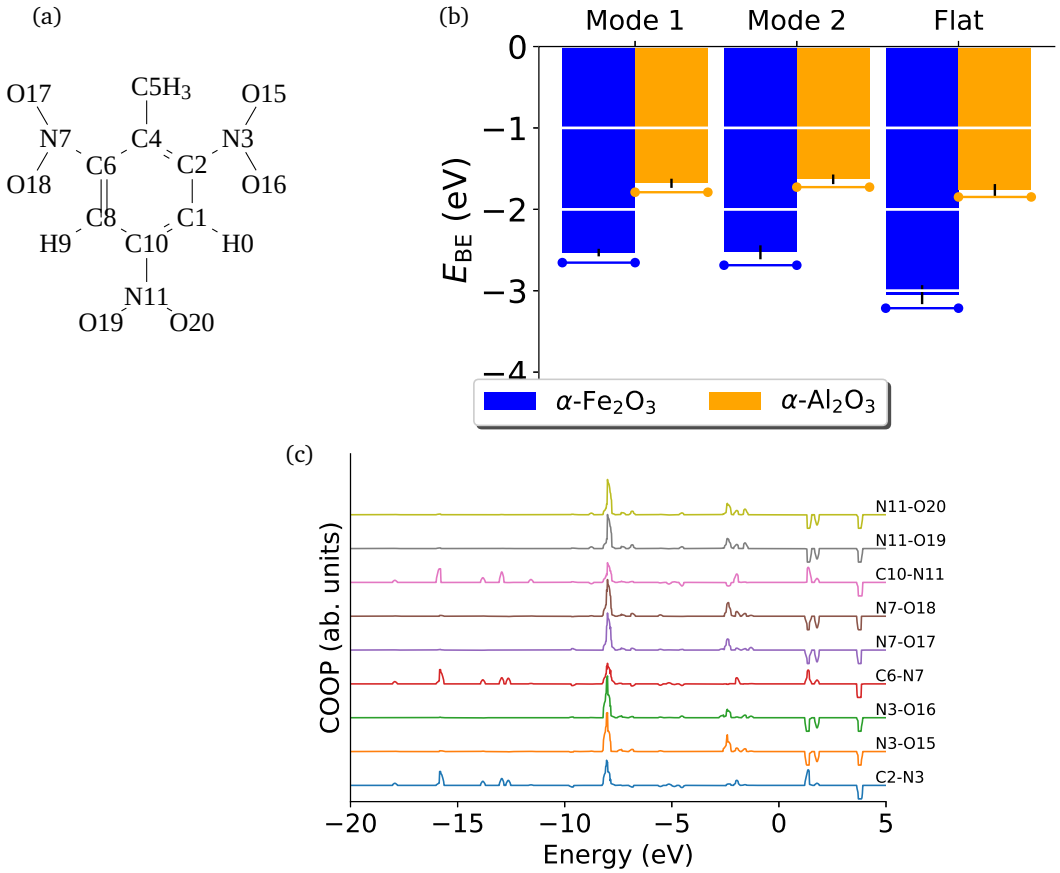

Fig. 4 (a) Schematic of 2,4,6-trinitrotoluene (TNT) with the atoms numbered, (b) mean binding energies for TNT on the α-Al_2O_3 (orange bars) and α-Fe_2O_3 (blue bars) surfaces. Vertical black lines on each bar denote the standard deviation with the binding modes labeled in Figure 3. Colored horizontal bars represent the binding energy for the lowest energy orientation. Numerical values are provided in Table S2 of the ESI.†, and (c) COOP curves for the gas-phase TNT. From Equation 4, negative peaks represent anti-bonding interactions whilst positive peaks represent bonding interactions.

3.2.2 5-nitro-2,4-dihydro-3H-1,2,4-triazol-3-one (NTO)

Similar to TNT and DNAN, 5-nitro-2,4-dihydro-3H-1,2,4-triazol-3-one (NTO) is a cyclic molecule; however, in contrast to the previous molecules, NTO features a five membered heterocyclic ring containing carbon and nitrogen. This heterocyclic ring is functionalized with a single $–NO_2$ and carbonyl group (see Figures 3c and 7a). This atomic orientation presents us with two vertical binding modes: one through the $–NO_2$ oxygens, and a second through the carbonyl group. The mean binding energies of these two modes in addition to the "flat" binding mode are presented in Figure 7b. Here, it should be noted that the "flat" orientation refers to the initial orientation in the complex. Upon optimization, NTO assumes a bidentate orientation where the plane of the molecule is perpendicular to the surface and NTO is bound through both the carbonyl and nitro moeties.

From Tables S9 and S11 of the ESI†, it is readily apparent for the lowest energy "flat" configuration that one of the N–H bonds (N0–H6 or N4–H10 in Figure 7a) experiences a radical change in bond length. Analysis of the structures reveals that NTO adsorbs to the α-Fe_2O_3 and α-Al_2O_3 surfaces whereby a proton attached to a ring nitrogen is transfered to a surface oxygen. The deprotonation of NTO upon adsorption has been previously observed for α-Al_2O_3 [20]; however in that study only the "flat" initial binding mode resulted in the deprotonation of NTO on α-Al_2O_3 (0001). In contrast, the current study shows deprotonation occurs on α-Fe_2O_3 (0001) surface for both binding mode 1 and the "flat" initial mode.

Moreover, examination of the minima hopping calculations reveals that only one configuration of NTO–α-Al_2O_3 resulted in deprotonation whilst for NTO–α-Fe_2O_3 a total of 16 orientations resulted in deprotonation of NTO (six for binding mode 1 and ten for the "flat" initial mode). This enhanced degree of deprotonation is in line with the observed acidities in Section 3.1; as the Fe^{+3} sites are more acidic than the Al^{+3} sites, the surface oxygens on the α-Fe_2O_3 (0001) would be a stronger conjugate Lewis base than those on the α-Al_2O_3 (0001) surface. Consequently, the α-Fe_2O_3 surface is more likely to accept a proton than the α-Al_2O_3 surface. This results in two sets of binding energies for mode 1 for the α-Fe_2O_3 (0001) and "flat" initial mode for both surfaces in Figure 7b: a neutral peak, and a deprotonated peak. For mode 1 on α-Fe_2O_3, we can readily see from Figure 7 that the binding energies for the neutral vs. deprotonated are similar to each other (within a standard deviation). However, for the "flat" mode, there is a clear trend of favoring the deprotonation of NTO for both surfaces, with deprotonation being $\sim$1 eV lower in energy than the neutral structures. These results indicate that under conditions in

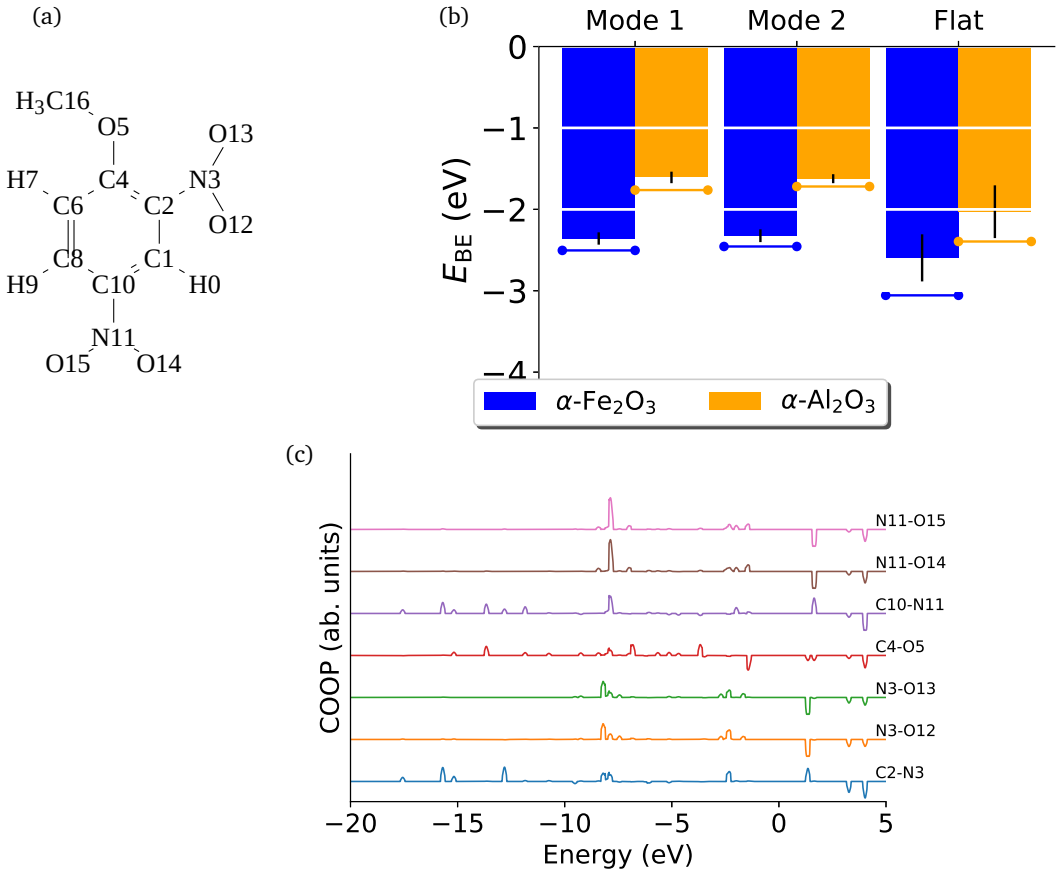

Fig. 5 (a) Schematic of 2,4-dinitroanisole (DNAN) with the atoms numbered, (b) mean binding energies for DNAN on the α-Al_2O_3 (orange bars) and α-Fe_2O_3 (blue bars) surfaces. Vertical black lines on each bar denote the standard deviation with the binding modes labeled in Figure 3. Colored horizontal bars represent the binding energy for the lowest energy orientation. Numerical values are provided in Table S2 of the ESI.†, and (c) COOP curves for the gas-phase DNAN. From Equation 4, negative peaks represent anti-bonding interactions whilst positive peaks represent bonding interactions.

which the "flat" mode dominates NTO will deprotonate and take on an ionic character.

Focusing on the lowest energy structure, we see from Table 3 that all adsorbates donate more electronic charge density to the α-Fe_2O_3 (0001) surface than to the α-Al_2O_3 (0001) surface. Moreover, NTO in the flat orientation shows the maximum amount of charge transfer. While TNT in the flat mode shows the same amount of charge transferred on α-Fe_2O_3 (0001) as NTO, it should be noted that TNT interacts *via* three Fe atoms while NTO interacts only through two. The maximum charge transfer showed by NTO can be attributed to the fact that in these surface bound complexes, NTO takes on more of an anionic form (*i.e.*, NTO donates a proton to a surface oxygen), and consequently this facilitates the larger amount of charge transfer to the surface as shown in Table 3.

Finally, the C=O and N–O bonds in contact with the M^{+3} metal sites elongate relative to the gas-phase, whilst the neighboring C–N bonds contract (see Figure 8 and Tables S9–S11 of the ESI†). Akin to the results for TNT and DNAN, an analysis of the COOP curves in Figure 7c reveals that for the C=O and N–O bonds in NTO, the molecular orbitals near the HOMO level are bonding in nature; thus as charge density is depleted from these orbitals, the overall bond order would decrease and the bond would elongate. Conversely, for the C–N bonds, the HOMO level is more anti-bonding in nature, and as a consequence, charge depletion of these orbitals results in a contraction of the bond. Similar to TNT and DNAN, these charge depletions/accumulations are readily visualized by the charge density differences in Figures S3 and S7 of the ESI†. Here, we can readily see the N–O bonds show a depletion of charge, which is in line with the COOP analysis.

3.2.3 Nitroguanidine (NQ)

Unlike the previous three munition compounds, nitroguanidine (NQ) is not cyclic; nonetheless, it does feature a $–NO_2$ group and two $–NH_2$ groups (Figures 3d and 9a), which presents two binding modes in addition to the "flat" mode, *i.e.*, one through the $–NO_2$ group (mode 1), and one through a terminal (or symmetrical equivalent) $–NH_2$ group (mode 2). It should be noted that similar to NTO, the label of "flat" refers to the initial configuration; upon adsorption NQ assumes more of a tilted configuration with binding occuring through the nitro and one of the amine groups. The mean binding energies with respect to these three binding modes are presented in Figure 9b. Interestingly, binding mode 2 of α-Al_2O_3 (0001) surface features a deprotonated NQ as its preferred binding mode with deprotonation increasing the stability of the NQ complex by $\sim$ 1.1 eV relative to the neutral form.

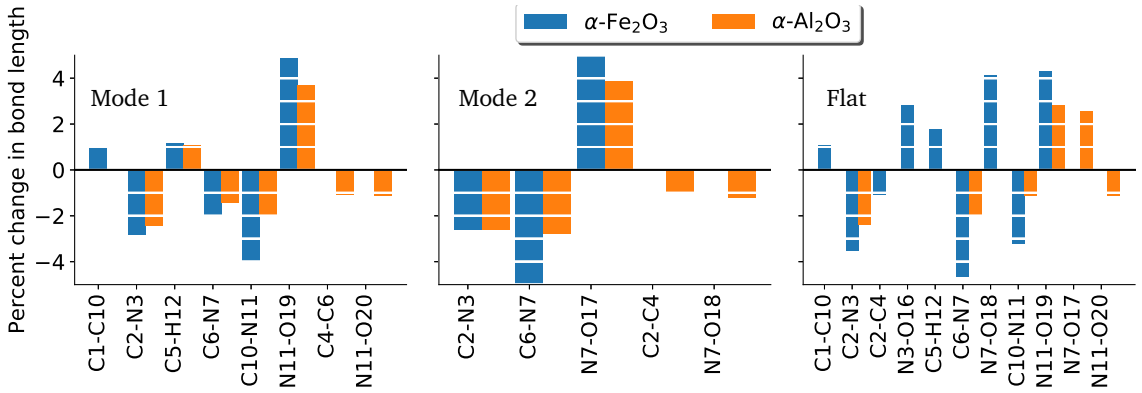

(a) 2,4,6-trinitrotoluene (TNT)

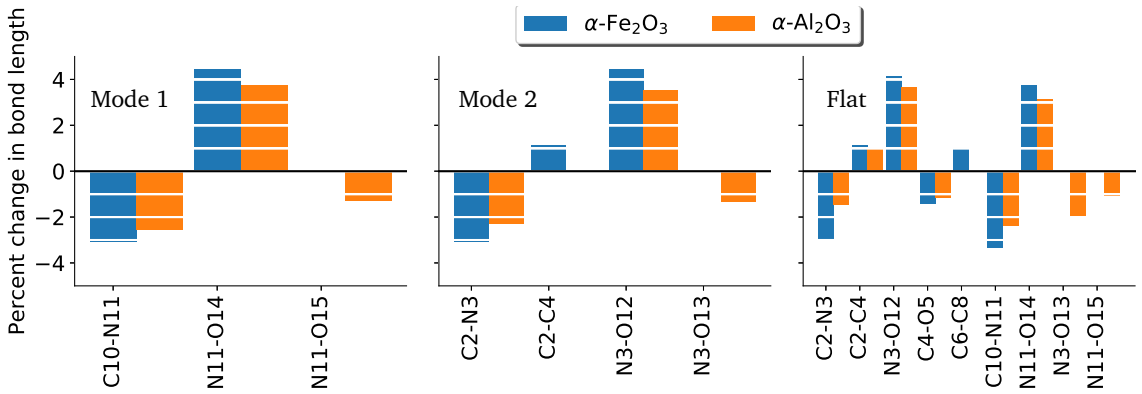

(b) 2,4-Dinitroanisole (DNAN)

Fig. 6 Percent change in the bond lengths from the gas-phase to the adsorbed phase for the munition compounds TNT and DNAN in different orientations. Negative percent change denotes the bond contracting relative to the gas-phase, whilst a positive percent change denotes the bond elongating relative to the gas-phase. Absolute percent changes less than 1% are not reported in this figure, and are available in Tables S3–S8 of the ESI†.

This is in contrast to the other orientations found for the other binding modes; here, the preferred form of NQ is the protonated form. It should be noted that while the minimum hopping algorithm found five deprotonated structures for the "flat" mode of NQ on the α-Fe_2O_3 (0001) surface, these structures were higher in energy by ~ 0.4 eV relative to the protonated structures, indicating that NQ prefers to stay protonated on the α-Fe_2O_3 (0001) surface.

Finally, we note that NQ displays a similar trend in the bond length changes observed for the previous three munition compounds, *i.e.*, N–O bonds lengthen, N–C and N–N bonds contract; this trend is explained via Figure 9c. Analogous to the prior munition compounds, the N–O bonds tend to be more bonding in nature near the HOMO level; thus, depletion of charge density from this region is accompanied by a decrease in bond order and an increase in bond length. Meanwhile, the N–C and N–N bonds are more anti-bonding in character near the HOMO level, which results in an increase in bond order and shorter bong lengths when charge is depleted. Visualization of the charge density differences in Figures S4 and S8 of the ESI† shows that the N–O bonds exhibit charge depletion, in line with the above analysis.

4 Discussion

While the four munition compounds considered in the current study vary in their molecular structure, some common trends are apparent. All compounds experienced the same N–O elongation effect, indicating a greater susceptibility for the $–NO_2$ groups to be transformed to amine ($–NH_2$), nitroso (–NO) or –NOOH groups, in line with experimental observations[13–19]. While it would be natural to assume that α-Fe_2O_3 would more readily carry out the reduction of the $–NO_2$ groups, it is worth noting that the differences in the Lewis acidity are similar to what was found for different facets of γ-Al_2O_3; here, a ~ 1 eV shift in the E_s^* descriptor resulted in ~ 0.3 eV shift in the reaction barrier for reducing alcohols[45]. Comparison of the E_s^* descriptor in Table 2 reveals there is a ~ 1.7 eV difference between α-Fe_2O_3 and α-Al_2O_3; utilization of the linear scaling relationships for γ-Al_2O_3 indicates that this would correspond to a change in the reaction barriers of ~ 0.8 eV. While obviously an estimate that bears further validation, this type of estimation indicates that while α-Fe_2O_3 is more reactive, the key difference between α-Fe_2O_3 and α-Al_2O_3 is not whether or not the reaction occurs, but rather the speed at which the reaction occurs. While a full understanding of the reactivity of these munition compounds is needed in order to determine their overall fate, a detailed kinetic study is beyond the scope of the current

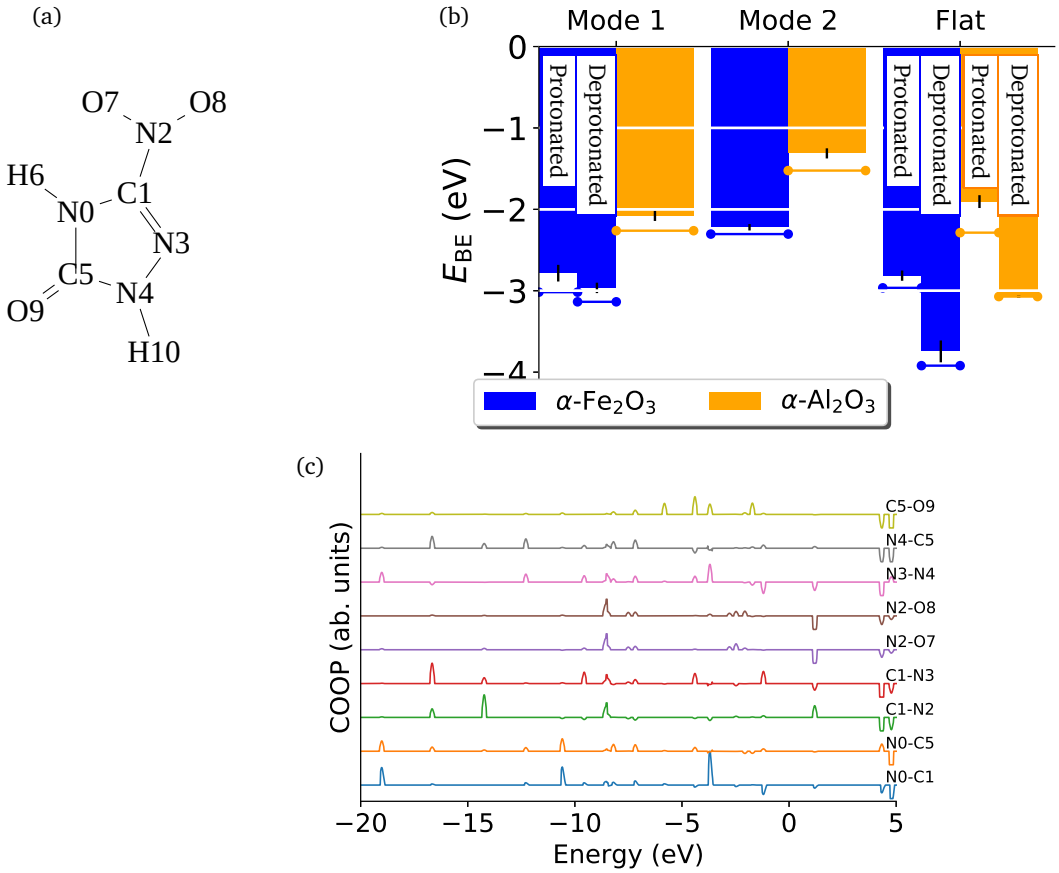

Fig. 7 (a) Schematic of 5-nitro-2,4-dihydro-3H-1,2,4-triazol-3-one (NTO) with the atoms numbered, (b) mean binding energies for 5-nitro-2,4-dihydro-3H-1,2,4-triazol-3-one (NTO) on the α-Al_2O_3 (orange bars) and α-Fe_2O_3 (blue bars) surfaces. Vertical black lines on each bar denote the standard deviation with the binding modes labeled in Figure 3. Colored horizontal bars represent the binding energy for the lowest energy orientation. Numerical values are provided in Table S2 of the ESI.†, and (c) COOP curves for the gas-phase NTO. From Equation 4, negative peaks represent anti-bonding interactions whilst positive peaks represent bonding interactions.

work, and will be the focus of a future study.

It should be noted that the current study neglects the effect of surface hydroxylation. Based on prior work from from our group, in the limit of a fully hydroxylated surface the interaction between a munition compound and the surface is described in terms of a van der Waals interaction rather than a Lewis acid-base interaction[22]. Conversely it has been demonstrated for ethanol that if the surface is partially hydroxylated, then the Lewis acid character of the adsorbate-surface interaction is preserved with the effect being greatly reduced. This results in a decreased binding energy between the adsorbate and the surface and increased reaction energetics[45]. Consequently, the effect of surface hydroxylation is dependent on the degree of hydroxylation, which in turn depends on the relative humidity of the environment being modeled.

5 Conclusions

In the current study, the Lewis acidity of two oxides (*i.e.*, α-Fe_2O_3 and α-Al_2O_3) common to arid soil was assessed with density functional theory (DFT). Through an analysis of the density of states and the binding of carbon monoxide, it was found that α-Fe_2O_3 is more Lewis acidic of the two oxides and as a result would more strongly interact with the electron rich moieties of the munition compounds (*i.e.*, 2,4,6-trinitrotoluene (TNT), 2,4-dinitroanisole (DNAN), 5-nitro-2,4-dihydro-3H-1,2,4-triazol-3-one (NTO), and nitroguanidine (NQ)). Application of the minima hopping algorithm allowed for the exploration of the complex potential energy surfaces of the four compounds, resulting in a total of 509 structures. Calculation of the binding energies reveals that α-Fe_2O_3 does bind the munition compounds more strongly than α-Al_2O_3. Analysis of the structures and density of states for the compounds reveals that the $-NO_2$ bonds are largely bonding in character near the HOMO level; thus as the Lewis acid M^{+3} sites deplete charge density from these molecular orbitals, the bond order for these bonds would decrease and the inter-atomic distances would increase. While this effect was observed for both oxides, α-Fe_2O_3 had a greater degree of elongation compared to α-Al_2O_3. Moreover, NTO more readily deprotonates in the presence of α-Fe_2O_3 than it does in the presence of α-Al_2O_3. The tendency of decreasing bond order for the $-NO_2$ group(s) indicates these moieties to be susceptible to transformation to amine ($-NH_2$), nitroso (–NO), or –NOOH groups.

Conflicts of interest

There are no conflicts to declare.

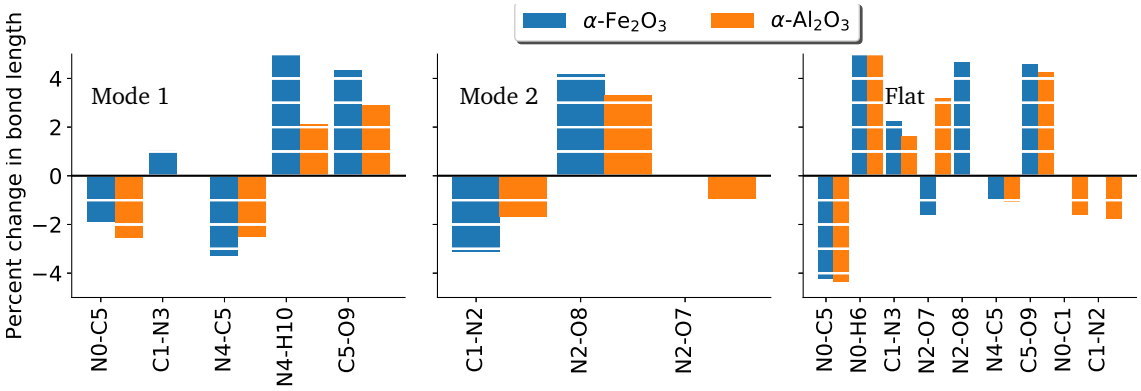

Fig. 8 Percent change in the bond lengths from the gas-phase to the adsorbed phase for the munition compound NTO in different orientations. Negative percent change denotes the bond contracting relative to the gas-phase, whilst a positive percent change denotes the bond elongating relative to the gas-phase. Absolute percent changes less than 1% are not reported in this figure, and are available in Tables S9–S11 of the ESI†. Bond labels correspond to the labeling scheme in Figure 7.

Acknowledgements

G.R.J. would like to acknowledge Mr. Jonathon Lym for his assistance with the density of states analysis. The authors also acknowledge Dr. Harley R. McAlexander and Dr. Timothy C. Schutt for their input on the manuscript. Furthermore, the use of trade, product, or firm names in this report is for descriptive purposes only and does not imply endorsement by the U.S. Government. The tests described and the resulting data presented herein, unless otherwise noted, were obtained from research conducted under the Environmental Quality Technology Program of the United States Army Corps of Engineers and the Environmental Security Technology Certification Program of the Department of Defense by the USAERDC. Permission was granted by the Chief of Engineers to publish this information. The findings of this report are not to be construed as an official Department of the Army position unless so designated by other authorized documents. This work was supported by a grant of computer time from the DOD High Performance Computing Modernization Program at ERDC, Vicksburg. This document has been approved for public release (Distribution Statement A).

Notes and references

1 M. E. Walsh, C. M. Collins, C. H. Racine, T. F. Jenkins, A. B. Gelvin and T. A. Ranney, *Sampling for Explosives Residues at Fort Greely: Alaska Reconnaissance Visit*, ERDC Technical Report July 2000, 2000.

2 F. Monteil-Rivera, A. Halasz, C. Groom, J.-S. Zhao, S. Thiboutot, G. Ampleman and J. Hawari, *Ecotoxicol. Explos. Unexplosed Ordance*, CRC Press, Taylor and Francis Group LLC, Boca Raton, FL, 2009, pp. 5–33.

3 A. Halasz, C. Groom, E. Zhou, L. Paquet, C. Beaulieu, S. Deschamps, A. Corriveau, S. Thiboutot, G. Ampleman, C. Dubois and J. Hawari, *J. Chromatogr. A*, 2002, **963**, 411–418.

4 J. Pichtel, *Appl. Environ. Soil Sci.*, 2012, **2012**, 1–33.

5 P. Nortier, P. Fourre, A. B. M. Saad, O. Saur, J. C. Lavalley, A. B. Mohammed, J. C. Lavalley, A. B. M. Saad, O. Saur and J. C. Lavalley, *Appl. Catal.*, 1990, **61**, 141–160.

6 A. Stakheev and L. Kustov, *Appl. Catal. A Gen.*, 1999, **188**, 3–35.

7 J. H. Clark, *Acc. Chem. Res.*, 2002, **35**, 791–797.

8 A. Corma and H. García, *Chem. Rev.*, 2003, **103**, 4307–65.

9 G. Busca, *Adv. Catal.*, Elsevier Inc., 1st edn, 2014, vol. 57, ch. 3, pp. 319–404.

10 J. C. Oxley, J. L. Smith, J. Yue and J. Moran, *Propellants, Explos. Pyrotech.*, 2009, **34**, 421–426.

11 L. Sviatenko, L. Gorb, F. Hill, D. Leszczynska, M. Shukla, S. Okovytyy, D. Hovorun and J. Leszczynski, *Environ. Sci. Technol.*, 2016, **50**, 10039–10046.

12 L. K. Sviatenko, L. Gorb, F. C. Hill, D. Leszczynska and J. Leszczynski, *J. Phys. Chem. A*, 2015, **119**, 8139–8145.

13 J. Heil, H. Vereecken and N. Brüggemann, *Eur. J. Soil Sci.*, 2016, **67**, 23–39.

14 J. N. Galloway, J. D. Aber, J. W. Erisman, S. P. Seitzinger, R. W. Howarth, E. B. Cowling and B. J. Cosby, *Bioscience*, 2003, **53**, 341.

15 F. Ahmad and J. B. Hughes, *Environ. Sci. Technol.*, 2002, **36**, 4370–4381.

16 H. Yin, T. K. Wood and B. F. Smets, *Appl. Microbiol. Biotechnol.*, 2005, **67**, 397–404.

17 C. L. Kitts, C. E. Green, R. A. Otley, M. A. Alvarez and P. J. Unkefer, *Can. J. Microbiol.*, 2000, **46**, 278–282.

18 C. I. Olivares, L. Abrell, R. Khatiwada, J. Chorover, R. Sierra-Alvarez and J. A. Field, *J. Hazard. Mater.*, 2016, **304**, 214–221.

19 T. Tang, Z. Yue, J. Wang, T. Chen and C. Qing, *J. Hazard. Mater.*, 2018, **343**, 176–180.

20 M. K. Shukla and F. Hill, *J. Phys. Chem. C*, 2014, **118**, 310–319.

21 M. K. Shukla and F. Hill, *J. Phys. Chem. C*, 2013, **117**, 13136–13142.

22 M. K. Shukla, J. Wang and J. Seiter, *J. Phys. Chem. C*, 2017, **121**, 11560–11567.

23 S. Goedecker, *J. Chem. Phys.*, 2004, **120**, 9911–9917.

24 A. a. Peterson, *Top. Catal.*, 2013, **57**, 40–53.

25 J. Enkovaara, C. Rostgaard, J. J. Mortensen, J. Chen,

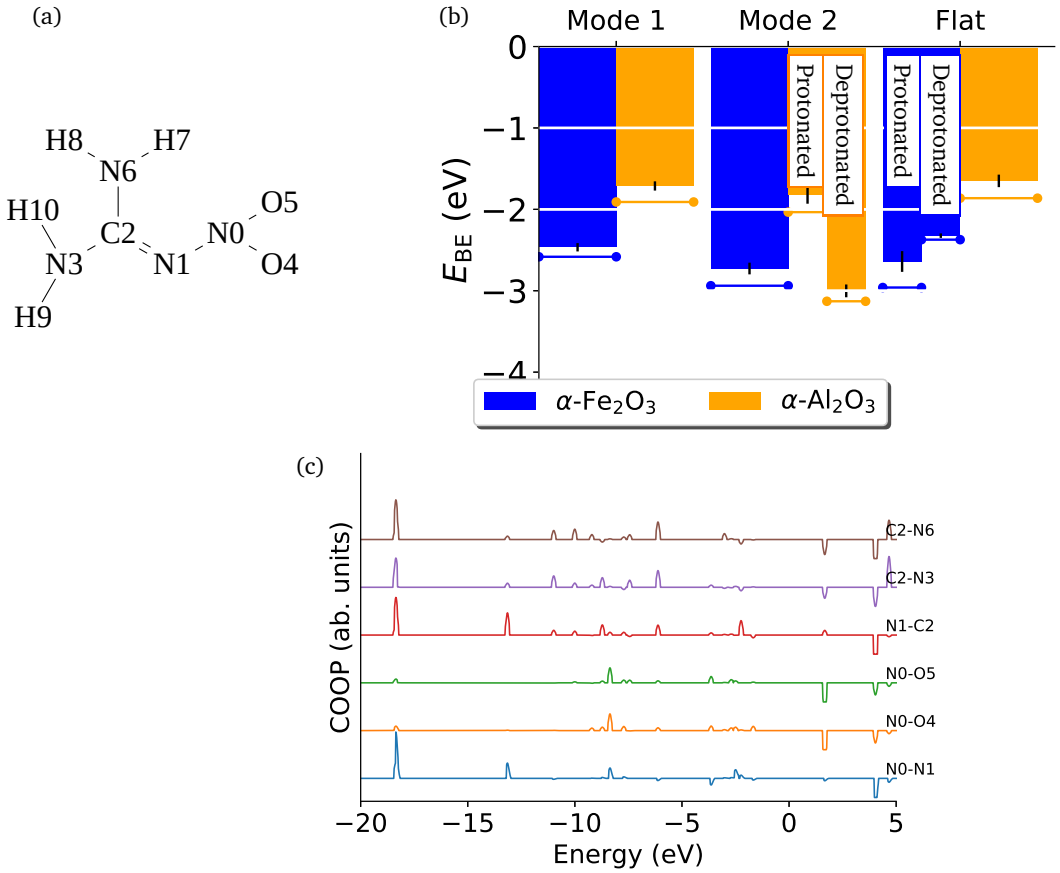

Fig. 9 (a) Schematic of nitroguanidine (NQ) with the atoms numbered, (b) mean binding energies for nitroguanidine (NQ) on the α-Al_2O_3 (orange bars) and α-Fe_2O_3 (blue bars) surfaces. Vertical black lines on each bar denote the standard deviation with the binding modes labeled in Figure 3. Colored horizontal bars represent the binding energy for the lowest energy orientation. Numerical values are provided in Table S2 of the ESI.†, and (c) COOP curves for the gas-phase NQ. From Equation 4, negative peaks represent anti-bonding interactions whilst positive peaks represent bonding interactions.

M. Dułak, L. Ferrighi, J. Gavnholt, C. Glinsvad, V. Haikola, H. a. Hansen, H. H. Kristoffersen, M. Kuisma, a. H. Larsen, L. Lehtovaara, M. Ljungberg, O. Lopez-Acevedo, P. G. Moses, J. Ojanen, T. Olsen, V. Petzold, N. a. Romero, J. Stausholm-Møller, M. Strange, G. a. Tritsaris, M. Vanin, M. Walter, B. Hammer, H. Häkkinen, G. K. H. Madsen, R. M. Nieminen, J. K. Nørskov, M. Puska, T. T. Rantala, J. Schiøtz, K. S. Thygesen and K. W. Jacobsen, *J. Phys. Condens. Matter*, 2010, **22**, 253202–253226.

26 A. H. Larsen, J. J. Mortensen, J. Blomqvist, I. E. Castelli, R. Christensen, M. Dułak, J. Friis, M. N. Groves, B. Hammer, C. Hargus, E. D. Hermes, P. C. Jennings, P. B. Jensen, J. Kermode, J. R. Kitchin, E. L. Kolsbjerg, J. Kubal, K. Kaasbjerg, S. Lysgaard, J. B. Maronsson, T. Maxson, T. Olsen, L. Pastewka, A. Peterson, C. Rostgaard, J. Schiøtz, O. Schütt, M. Strange, K. S. Thygesen, T. Vegge, L. Vilhelmsen, M. Walter, Z. Zeng and K. W. Jacobsen, *J. Phys. Condens. Matter*, 2017, **29**, 273002.

27 J. Mortensen, L. Hansen and K. Jacobsen, *Phys. Rev. B*, 2005, **71**, 035109.

28 J. P. Perdew, K. Burke and M. Ernzerhof, *Phys. Rev. Lett.*, 1996, **77**, 3865–3868.

29 P. E. Blöchl, *Phys. Rev. B*, 1994, **50**, 17953–17979.

30 G. Kresse, *Phys. Rev. B*, 1999, **59**, 1758–1775.

31 P. Pulay, *Chem. Phys. Lett.*, 1980, **73**, 393–398.

32 D. M. Wood and A. Zunger, *J. Phys. A. Math. Gen.*, 1985, **18**, 1343–1359.

33 R. Rivera, H. P. Pinto, A. Stashans and L. Piedra, *Phys. Scr.*, 2012, **85**, 015602.

34 D. C. Liu and J. Nocedal, *Math. Prog.*, 1989, **45**, 503–528.

35 A. H. Larsen, M. Vanin, J. J. Mortensen, K. S. Thygesen and K. W. Jacobsen, *Phys. Rev. B*, 2009, **80**, 195112–1 – 195112–10.

36 G. R. Jenness and D. G. Vlachos, *J. Phys. Chem. C*, 2015, **119**, 5938–5945.

37 R. Bader, *Atoms in Molecules: A Quantum Theory*, Clarendon, Oxford, U. K., 1994.

38 G. Henkelman, A. Arnaldsson and H. Jónsson, *Comput. Mater. Sci.*, 2006, **36**, 354–360.

39 E. Sanville, S. D. Kenny, R. Smith and G. Henkelman, *J. Comput. Chem.*, 2007, **28**, 899–908.

40 W. Tang, E. Sanville and G. Henkelman, *J. Phys. Condens. Matter*, 2009, **21**, 084204.

41 T. Hughbanks and R. Hoffmann, *J. Am. Chem. Soc.*, 1983, **105**, 3528–3537.

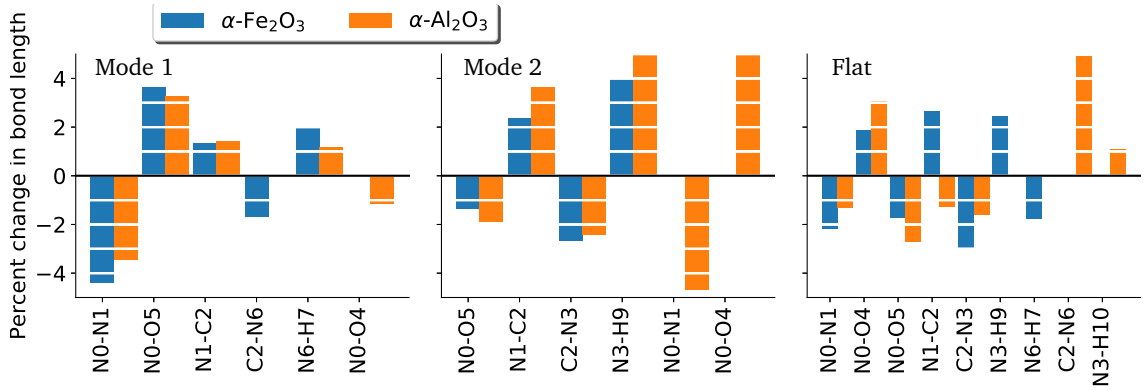

Fig. 10 Percent change in the bond lengths from the gas-phase to the adsorbed phase for the munition compound NQ in different orientations. Negative percent change denotes the bond contracting relative to the gas-phase, whilst a positive percent change denotes the bond elongating relative to the gas-phase. Absolute percent changes less than 1% are not reported in this figure, and are available in Tables S12–S13 of the ESI†.

42 J. Lewis, D. Schwarzenbach and H. D. Flack, *Acta Crystallogr. Sect. A*, 1982, **38**, 733–739.

43 Y. Maslen, E.N. Streltsov, V.A. Streltsova, N.R. Ishizawa, N. Satow, *Acta Crystallogr. Sect. B Struct. Sci.*, 1993, **49**, 973–980.

44 H. J. Monkhorst and J. D. Pack, *Phys. Rev. B*, 1976, **13**, 5188–5192.

45 G. R. Jenness, M. A. Christiansen, S. Caratzoulas, D. G. Vlachos and R. J. Gorte, *J. Phys. Chem. C*, 2014, **118**, 12899–12907.

46 G. R. Jenness, W. Wan, J. G. Chen and D. G. Vlachos, *ACS Catal.*, 2016, **6**, 7002–7009.

47 A. Corma, *Chem. Rev.*, 1995, **95**, 559–614.

48 R. C. Deka, R. Kinkar Roy and K. Hirao, *Chem. Phys. Lett.*, 2004, **389**, 186–190.

49 R. Hoffmann, *Solids and Surfaces: A chemist's view of bonding in extended structures*, VCH Publishers, Inc., New York, N. Y., 1988.

50 A. J. Stone, *The Theory of Intermolecular Forces*, Oxford University Press, Oxford, U. K., 2002nd edn, 1996.

51 D. S. Sholl and J. A. Steckel, *Density Functional Theory: A Practical Introduction*, John Wiley & Sons, Inc., Hoboken, NJ, USA, 2009.